Nano Research

Open Access

Research Article

Construction of type-II $BiVO_4$/FeCoMOF p–n heterojunction for enhanced photoelectrochemical water oxidation

Qingyuan Chen, Yu He, Jinkang Ge, Jing Zhang, Dongxu Wang, Chungui Tian, Aiping Wu ✉, and Honggang Fu ✉

Key Laboratory of Functional Inorganic Material Chemistry, Ministry of Education of the People's Republic of China, Heilongjiang University, Harbin 150080, China

Cite this article: *Nano Research*, **2026**, *19*, 94908454. https://doi.org/10.26599/NR.2026.94908454

ABSTRACT: Photoelectrochemical (PEC) water splitting is a highly promising approach for sustainable hydrogen production. $BiVO_4$ (BVO) possesses an appropriate bandgap and excellent optical properties; however, its poor carrier transport and sluggish water-oxidation kinetics severely limit the utilization of holes, leading to low PEC efficiency. Herein, we rationally design a p–n heterojunction with a stepwise type-II energy band configuration through the *in-situ* growth of p-type FeCoMOF on n-type BVO. This architecture promotes the efficient and selective separation of photogenerated electrons and holes, enabling the BVO/FeCoMOF photoanode to achieve enhanced PEC water oxidation performance. The optimized photoanode delivers a remarkable photocurrent density of 6.2 mA·cm^{-2} at 1.23 V vs. reversible hydrogen electrode (RHE) under AM 1.5 G illumination, which is 3.8 times higher than that of bare BVO photoanode, and exhibits significantly enhanced operational stability compared to the bare BVO. Furthermore, gas-evolution tests confirm highly stoichiometric water splitting, yielding an H_2/O_2 ratio close to 2:1, along with a Faradaic efficiency exceeding 92%. Detailed physicochemical characterization, including intensity-modulated photocurrent spectroscopy (IMPS), intensity-modulated photovoltage spectroscopy (IMVS), and *in-situ* Kelvin probe force microscopy (KPFM), confirm that the construction of the type-II p–n heterojunction effectively promotes the hole transfer from BVO to the FeCoMOF layer, enhances the charge-separation efficiency, and prolongs the carrier lifetime. Furthermore, the FeCoMOF modification significantly reduces the interfacial reaction resistance and enhances the charge utilization efficiency, thereby further improving the PEC performance. This work provides new insights into the rational design of high-performance photoelectrode.

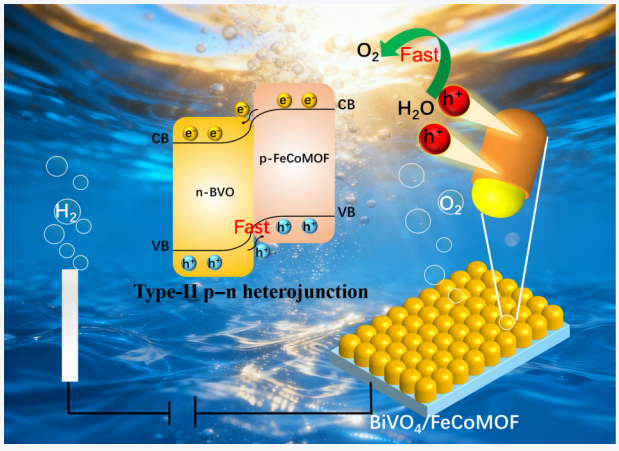

KEYWORDS: photoelectrochemical water splitting, bismuth vanadate, metal organic framework, p–n heterojunction.

1 Introduction

Photoelectrochemical (PEC) technology operates under mild reaction conditions and directly converts solar energy into chemical energy, offering a promising pathway to address the increasing global demand for sustainable energy sources [1, 2]. Compared with traditional photocatalysis and electrocatalysis [3, 4], PEC water splitting integrates light absorption and electrochemical driving forces within a single system, which enhances the separation of light-generated charges and directs their transport to surface reaction sites, effectively suppressing charge recombination and resulting in superior charge utilization efficiency, while reducing the overpotential required for water splitting reactions compared to pure electrocatalysis. In PEC water splitting systems, the selection of photoanode materials is critical to the overall solar conversion efficiency, as it must drive the kinetically sluggish and multi-step oxygen evolution reaction (OER). Among candidate photoanode materials, $BiVO_4$ (BVO), with a suitable bandgap (~ 2.4 eV) and abundant raw material sources, has been widely applied in photoanode construction [5, 6]. However, the short carrier diffusion length and high interfacial recombination rate severely hinder further improvement of its PEC performance [7].

Received: December 11, 2025; **Revised:** January 13, 2026
Accepted: January 15, 2026

✉Address correspondence to Aiping Wu, wuaiping@hlju.edu.cn; Honggang Fu, fuhg@vip.sina.com; fuhg@hlju.edu.cn

At present, the main strategies to improve the PEC performance of BVO include: (i) tuning the band structure via element doping to improve the carrier transport efficiency and photogenerated charge separation rate [8, 9]; (ii) constructing heterostructures by combining BVO with suitable semiconductors, such as g-C_3N_4 [10, 11], WO_3 [12, 13], and Fe_2O_3 [14], to facilitate the spatial separation of photogenerated carriers; (iii) surface modification through the introduction of cocatalysts, such as Co-Pi and NiFeOOH [15–19], to reduce the kinetic barrier of the OER; (iv) applying external physical fields, such as electric or magnetic fields [20], to modulate charge transport pathways and alter interfacial reaction behaviors; and (v) utilizing the surface plasmon resonance (SPR) effect [19, 21–23], where the local light field enhancement of metal nanoparticles expands the light absorption range and boosts the charge excitation capability. Although these strategies have achieved remarkable progress, the intrinsic charge separation and utilization efficiency of BVO still remain unsatisfactory. Therefore, it is highly desirable to explore advanced heterostructures with stronger built-in fields and faster interfacial charge dynamics. Among various candidate materials, metal-organic frameworks (MOFs) have recently attracted considerable attention as efficient OER cocatalysts and heterojunction components, owing to their high surface area, tunable metal sites, and structural versatility. Recent studies have shown that ultrathin Co-based MOF (CoMOF) layers can effectively passivate surface trap states of BVO, suppress surface recombination, and thereby enhance interfacial charge transfer. Moreover, the metal sites in CoMOF facilitate the extraction and transfer of photogenerated holes from BVO, accelerating the hole transport at the semiconductor–electrolyte interface and reducing the bulk recombination [24, 25]. In addition to CoMOF, Fe-based MOFs (FeMOF) have also been widely employed, as they provide abundant active sites that promote the water adsorption and activation, and act as efficient hole-accumulation centers to enable more photogenerated holes to participate in the oxidation reaction, thereby improving overall OER kinetics [26]. Compared to monometallic MOFs, bimetallic MOFs with uniformly dispersed multimetal centers and tunable coordination environments can further optimize the water adsorption and activation, reduce the OER overpotential, and enhance the interfacial charge-transfer efficiency [27, 28]. Furthermore, Fe and Co are earth-abundant, cost-effective, and environmentally benign elements, making Fe/Co bimetallic MOF (FeCoMOF) an ideal choice for sustainable PEC applications. Therefore, integrating FeCoMOF with BVO to construct heterojunctions is expected to improve the charge separation and transport, ultimately enhancing the water oxidation efficiency.

In this study, we successfully loaded composition-tunable amorphous FeCoMOF on the surface of BVO photoanodes using a hydrothermal method, thereby creating an intimate p–n heterojunction interface. Upon contact between p-type FeCoMOF (hole-rich) and n-type BVO (electron-rich), the interdiffusion of charge carriers establishes a space-charge region across the interface, leading to the formation of a built-in electric field directed from the n-type BVO toward the p-type FeCoMOF. Under illumination, this built-in electric field serves as the primary electrostatic driving force, enabling the spatial separation of photogenerated charge carriers prior to their participation in surface reactions by directing electrons toward the BVO bulk and holes toward the FeCoMOF layer. On this basis, the stepwise type-II band alignment further provides a favorable energetic gradient, lowering the interfacial charge-transfer barrier and synergistically promoting the efficient and directional migration of photogenerated electrons and holes across the heterojunction interface. Meanwhile, the amorphous FeCoMOF layer, featuring abundant unsaturated metal sites and flexible coordination environments, further accelerates surface oxygen evolution kinetics. As a result, the BVO/FeCoMOF photoanode achieves synergistic enhancement in both charge separation efficiency and surface reaction kinetics for photoelectrochemical water oxidation. A significant enhancement in photocurrent density is observed for the BVO/FeCoMOF photoanode, reaching 6.23 mA·cm^{-2} at 1.23 V vs. reversible hydrogen electrode (RHE), which is 3.8 times that of the bare BVO (1.6 mA·cm^{-2}). A series of spectroscopic and electrochemical characterizations demonstrated the successful formation of the heterojunction and the enhancement of interfacial charge dynamics.

2 Results and discussion

2.1 Morphology and structure of BVO/FeCoMOF

The preparation process of the BVO/FeCoMOF photoanode is illustrated in Fig. 1(a). Firstly, the BVO photoanode was synthesized through a combination of electrodeposition and heat treatment. Subsequently, the fluorine-doped tin oxide (FTO) glass loaded with BVO was placed face-down at an angle of 45° in a stainless-steel autoclave containing a precursor solution of FeCoMOF. After hydrothermal reaction and washing, the BVO/FeCoMOF photoanode was obtained. The surface morphology of the pure BVO photoanode and the BVO/FeCoMOF photoanode was characterized by scanning electron microscopy (SEM). As shown in Fig. 1(b) and Fig. S1 in the Electronic Supplementary Material (ESM), the pure BVO exhibited uniformly grown cross-linked nanorods with smooth surfaces. After the deposition of FeCoMOF, the original morphology of BVO remained unchanged, while the surface became noticeably rougher (Fig. 1(c)). This roughened appearance confirms that the FeCoMOF is tightly anchored onto the BVO nanorods at the nanoscale. Such intimate nanoscale contact between the MOF and BVO enables the formation of an effective heterojunction interface, which facilitates interfacial charge separation and transfer during PEC operation. Transmission electron microscopy (TEM) was employed to further investigate the microstructural characteristics of the BVO/FeCoMOF photoanode. A distinct boundary can be clearly observed between BVO and FeCoMOF, confirming the formation of a well-defined heterojunction interface. The FeCoMOF region displays no discernible lattice fringes, suggesting an amorphous or poorly crystalline nature (Figs. 1(d) and 1(e)). In contrast, the BVO region exhibits clear lattice fringes with an interplanar spacing corresponding to the ($\bar{1}$21) plane of BVO, indicating its high crystallinity. The selected area electron diffraction (SAED) pattern displays a series of diffraction rings that can be indexed to the ($\bar{1}$21), ($\bar{1}$41), ($\bar{2}$31), (222), and (123) planes of BVO, further verifying its polycrystalline structure (Fig. S2 in the ESM). Furthermore, energy-dispersive X-ray spectroscopy (EDS) mapping analysis reveals a uniform distribution of Bi, V, Fe, Co, O, and C elements throughout the composite (Figs. 1(f)–1(k)). The homogeneous coexistence of Fe and Co signals further demonstrates the successful deposition of the FeCoMOF layer on the BVO surface. Meanwhile, the overlapping elemental distributions confirm the intimate

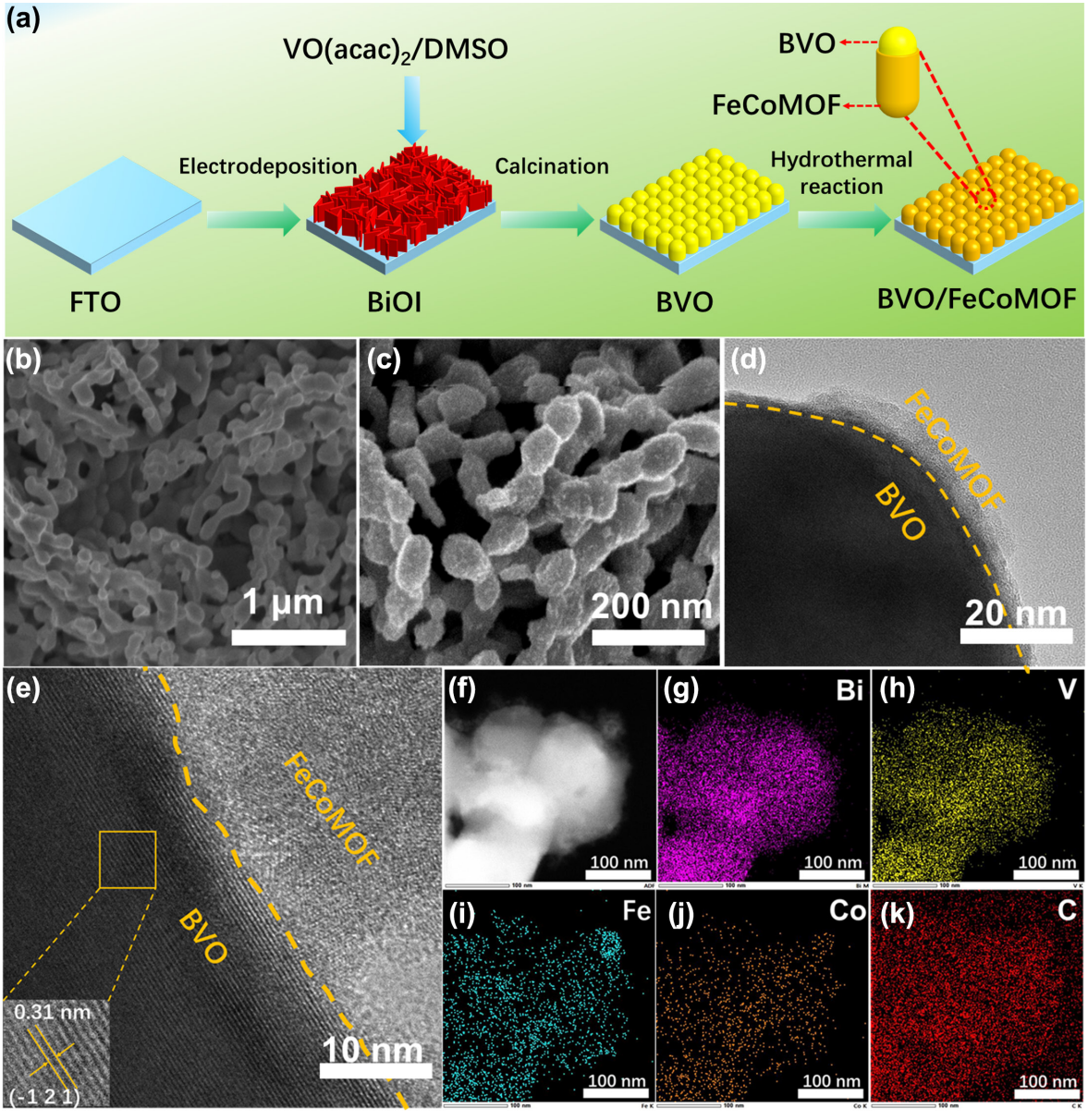

Figure 1 (a) Preparation process for BVO/FeCoMOF photoanode. ((b) and (c)) SEM images of BVO and BVO/FeCoMOF. ((d) and (e)) High-resolution TEM (HRTEM) images of BVO/FeCoMOF. ((f)–(k)) EDS element mappings of BVO/FeCoMOF.

interfacial contact between FeCoMOF and BVO, which is favorable for efficient charge separation and transfer during the PEC process. The phase composition of the samples was analyzed using X-ray diffraction (XRD). As displayed in Fig. 2(a), all diffraction peaks of BVO photoanode can be indexed to monoclinic BVO (JCPDS No. 14-0688) and SnO_2 (JCPDS No. 46-1088) [29], suggesting the successful preparation of BVO. After loading FeCoMOF, the main diffraction peaks of BVO remained unchanged, indicating that its crystal structure was not significantly disrupted. Meanwhile, no diffraction peaks attributed to FeCoMOF were observed, likely due to their amorphous nature or low crystallinity. However, both single-metal MOFs (FeMOF and CoMOF) exhibit distinct XRD diffraction peaks (Fig. S3 in the ESM), indicating well-defined crystal structures and high crystallinity.

To obtain more compositional and structural information, Raman spectroscopy and Fourier-transform infrared (FTIR) spectroscopy were conducted. As shown in Fig. 2(b), the peaks at 331 and 371 cm^{-1} are correspond to the symmetric and asymmetric bending vibration modes of the vanadate (VO_4^{3-}) tetrahedron, respectively. Additionally, the peak at 819 cm^{-1} is attributed to the symmetric stretching vibration mode of the V–O bond [30], further confirming the existence of monoclinic BVO. After the introduction of the FeCoMOF, these characteristic peaks remained, but a slight red shift in the peak positions was observed. Specifically, the symmetric stretching vibration peak of the V–O bond shifted from 819 to 826 cm^{-1}, indicating a shortening of the V–O bonds within the lattice of the BVO/FeCoMOF material, which may be related to the structural disturbance of the BVO surface lattice caused by the presence of the metal-organic framework layer. Notably, the results indicate that the incorporation of FeCoMOF did not damage the crystal structure of BVO, but it did alter the local surface environment to a certain extent. FTIR spectra (Fig. 2(c)) show that the pure BVO exhibited characteristic absorption peaks at 843 and 715 cm^{-1}, which are mainly attributed

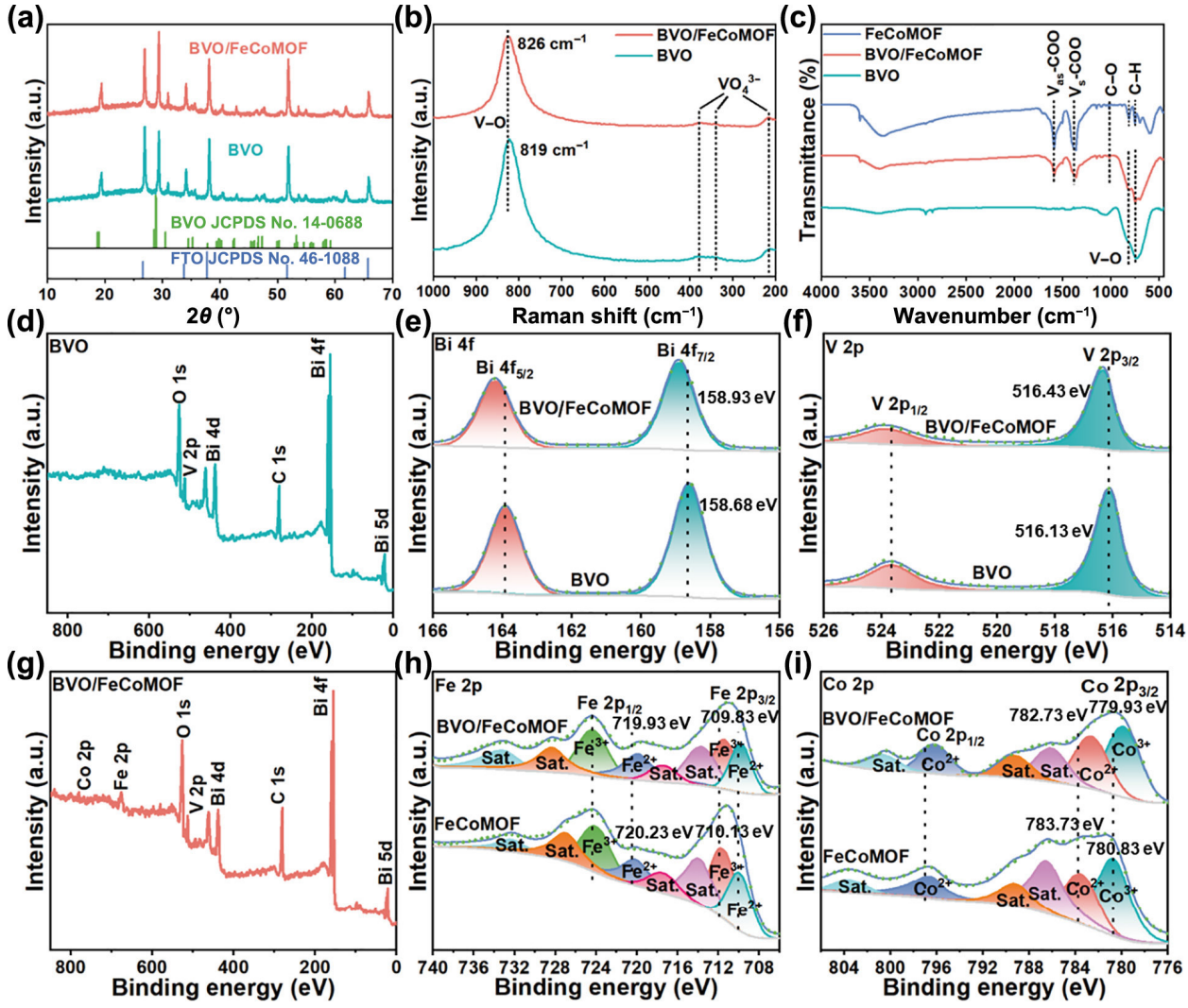

Figure 2 (a) XRD patterns of different samples. (b) Raman spectra of BVO and BVO/FeCoMOF photoanodes. (c) FTIR spectra of the BVO BVO/FeCoMOF and FeCoMOF. ((d)–(i)) Full XPS spectra and high-resolution Bi 4f, V 2p, Fe 2p, and Co 2p for BVO and BVO/FeCoMOF.

to the stretching vibrations of V–O bonds. The FeCoMOF, as a metal-organic framework material, displayed characteristic peaks primarily in the regions related to organic ligands and metal coordination. The peaks at 1566 and 1364 cm^{-1} correspond to the asymmetric and symmetric stretching vibrations of the carboxylate group (COO^-), respectively, indicating that the carboxylic acid groups coordinated with metal ions (Fe/Co) to form coordination complexes. The peak at 1001 cm^{-1} is attributed to the bending vibration of the C–O bond, while the peaks at 815 and 749 cm^{-1} correspond to the out-of-plane bending vibrations of C–H bonds, confirming the presence of aromatic rings [31]. After loading FeCoMOF onto BVO, the composite sample exhibited both the V–O stretching vibration peaks of BVO and the characteristic peaks of organic functional groups from FeCoMOF, further confirming that the MOF was successfully loaded onto the surface of BVO without significantly affecting its primary framework structure.

To further investigate the elemental composition and chemical states, X-ray photoelectron spectroscopy (XPS) measurements were carried out on pristine BVO, FeCoMOF, and the BVO/FeCoMOF composite. As shown in the survey spectra (Figs. 2(d) and 2(g), and Fig. S5 in the ESM), the presence of Bi, V, Fe, and Co elements in the composite sample is clearly evident, confirming the successful anchoring of FeCoMOF onto the surface of BVO. Figures 2(e)–2(i) show that the binding energies of Bi and V in the BVO/FeCoMOF composite shifted to higher values compared to those in pristine BVO, whereas the binding energies of Fe and Co reduced relative to those in pristine FeCoMOF. The changes in binding energy indicate that there is an interaction between BVO and FeCoMOF, with electrons transferring from BVO to FeCoMOF. The redistribution of electrons modulates the interfacial electronic structure and induces a built-in electric field directed from BVO toward FeCoMOF, thereby facilitating the separation and migration of photogenerated charge carriers, reducing their recombination probability at the interface, and providing more favorable reaction kinetics for subsequent water oxidation. Moreover, the high-resolution O 1s XPS spectrum of the BVO/FeCoMOF photoanode (Fig. S4 in the ESM) can be deconvoluted into four characteristic peaks located at 529.53, 530.48, 532.03, and 533.23 eV. The dominant peak at 529.53 eV is assigned to lattice oxygen (O_L) in BVO, while the peak at 530.48 eV corresponds to the C=O bonds originating from the organic ligands of the FeCoMOF. The peak at 532.03 eV is attributed to C–O species, and the weak feature at 533.23 eV is associated with surface-adsorbed oxygen species (O_C), such as hydroxyl groups or adsorbed H_2O.

2.2 Band structure analysis

The light absorption properties of the prepared photoanodes were evaluated using ultraviolet–visible diffuse reflectance spectroscopy (UV–vis DRS). Figure 3(a) shows that both the pure BVO and the BVO/FeCoMOF composite exhibited absorption edges around ~ 520 nm. Compared with pure BVO, the BVO/FeCoMOF composite demonstrated enhanced absorption in the range of 320–475 nm, indicating that the FeCoMOF possibly improved the light-harvesting ability of BVO. However, no obvious shifts in the absorption edge were observed, suggesting that FeCoMOF did not directly alter the electronic structure of BVO. Instead, it optimized the separation and migration of photogenerated charge carriers through interfacial interactions. To further estimate the bandgap values of the samples, Tauc transformations were applied to the diffuse reflectance data, as shown in Figs. 3(b)–3(d). The bandgap of pure BVO was approximately 2.52 eV, whereas the bandgap of the BVO/FeCoMOF composite slightly decreased to around 2.50 eV. This slight decrease in bandgap may be attributed to charge redistribution effects induced by the FeCoMOF, which could facilitate the migration of photogenerated electrons and enhance their participation in catalytic reactions [24]. These results indicate that the introduction of FeCoMOF not only improved the light absorption capability but also potentially reduced the recombination rate of electrons and holes, thereby enhancing photoelectrocatalytic activity. To further obtain band information, Mott–Schottky (M–S) measurements were conducted at a frequency of 1 kHz for BVO, FeCoMOF, and BVO/FeCoMOF photoelectrodes. As shown in Figs. 3(e) and 3(f), the M–S plot of BVO exhibits a positive slope, indicating typical n-type semiconductor behavior, whereas FeCoMOF displays a negative slope, characteristic of p-type conductivity. Upon coupling, the BVO/FeCoMOF electrode presents a distinct inverted V-shaped curve, confirming the successful formation of a p–n heterojunction interface. Because the slope of the M–S plot is inversely proportional to the donor density (N_d) [32–34], the smaller slope observed for BVO/FeCoMOF implies a higher carrier concentration ($N_{d\ BVO/FeCoMOF} > N_{d\ BVO}$). This increased carrier density indicates that the incorporation of FeCoMOF significantly enhances the electron conductivity and charge transfer capability of the photoanode [35], thereby facilitating efficient charge separation and transport. The extrapolated intercept of the M–S plot on the

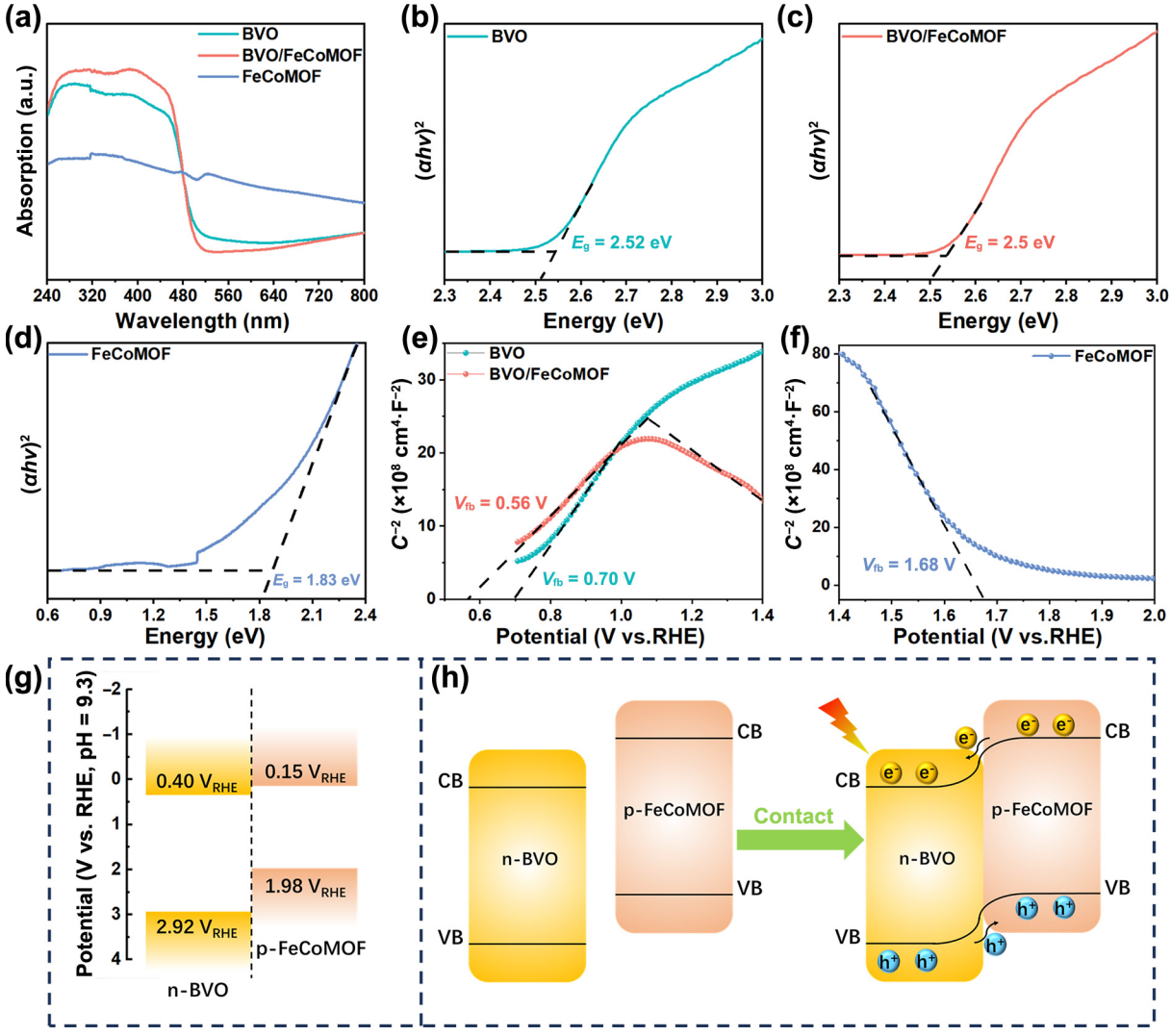

Figure 3 (a) UV–vis absorption spectra of BVO, BVO/FeCoMOF, and FeCoMOF. ((b)–(d)) Tauc plot of BVO, BVO/FeCoMOF, and FeCoMOF. ((e) and (f)) M–S curves of BVO, BVO/FeCoMOF, and FeCoMOF. (g) Schematic diagram of band positions of BVO and FeCoMOF. (h) Schematic diagram of the charge carrier transfer process.

potential axis corresponds to the flat-band potential (V_{fb}), which reflects the degree of band bending [36–39]. The pronounced negative shift in V_{fb} after FeCoMOF loading suggests a stronger internal electric field and enhanced band bending, which provide a larger driving force for photogenerated hole migration. The flat-band potentials of BVO and FeCoMOF are determined to be 0.70 and 1.68 V vs. RHE, respectively. Based on these values, the valence and conduction band edges of BVO are calculated to be 2.92 and 0.40 V vs. RHE, while those of FeCoMOF are 1.98 and 0.15 V vs. RHE, respectively (Fig. 3(g)). As shown in Fig. 3(h), when the two materials exist separately, each maintains its intrinsic conduction band and valence band positions. Because the CB and VB of BVO lie below those of FeCoMOF, a typical type-II band alignment is established between them. Upon contact, Fermi level equilibration occurs at the interface between the n-type and p-type semiconductors, leading to the band bending and the formation of a built-in electric field directed from the n-type to the p-type semiconductor, thereby constructing a p–n heterojunction. This built-in electric field further enhances the driving force for the migration of photogenerated charge carriers in the type-II band configuration. Under illumination, the type-II band offset together with the built-in electric field drives photogenerated electrons to transfer from the CB of FeCoMOF to that of BVO, while photogenerated holes migrate from the VB of BVO to that of FeCoMOF. Such directional charge transfer effectively suppresses interfacial recombination, thereby significantly improving the PEC conversion efficiency. Such well-aligned band structures effectively straddle the redox potential of O_2/H_2O, enabling efficient visible-light-driven OER. Notably, the charge-transfer mechanism governed by the combined p–n junction effect and type-II band offset is fundamentally distinct from conventional surface-passivation or cocatalyst-modification strategies. The latter typically suppresses the carrier recombination by reducing surface defect states or accelerating interfacial reaction kinetics, with their influence largely confined to the electrode/electrolyte interface. In contrast, the p–n heterojunction constructed in this work introduces a stable built-in electric field within the semiconductor framework, enabling effective carrier separation at the bulk/interface level prior to surface reactions. The stepwise type-II band alignment further facilitates directional electron–hole transfer, effectively lowering the energy barrier for carrier migration and enhancing overall charge separation efficiency.

2.3 PEC water splitting performance

The PEC water oxidation performance of the fabricated photoanodes was evaluated in a 0.5 M potassium borate (KBi) electrolyte (pH = 9.3) under AM 1.5 G simulated solar irradiation. To ensure a stable reaction temperature and eliminate the influence of thermal fluctuations during the measurements, the PEC cell was coupled with a circulating water system. As shown in Fig. 4(a), the bare BVO photoanode displayed a relatively low photocurrent density of 1.6 mA·cm^{-2} at 1.23 V vs. RHE, which is attributed to its sluggish interfacial charge transfer kinetics, leading to severe recombination of photogenerated carriers. To overcome these limitations, a series of single and bimetallic MOFs were introduced onto the BVO surface. After modification, both BVO/FeMOF and BVO/CoMOF photoanodes showed enhanced photocurrent densities of 3.2 and 2.1 mA·cm^{-2}, respectively, indicating that the incorporation of transition-metal MOFs can effectively promote surface reaction kinetics. More notably, the BVO/FeCoMOF photoanode demonstrates the best performance, suggesting that the synergy between Fe and Co further accelerates the kinetics of the catalytic reaction. As illustrated in Fig. S6 in the ESM, the PEC activity exhibited a strong dependence on the Fe/Co ratio. The photocurrent density gradually increased with increasing Fe content, reaching a maximum of 6.2 mA·cm^{-2} for BVO/Fe_4Co_1MOF at 1.23 V vs. RHE, which is approximately 3.8 times higher than that of pristine BVO and 1.9 times higher than that of BVO/FeMOF. Additionally, the hydrothermal reaction time also has a significant impact on catalytic performance, and the sample with a reaction time of 48 h has the best performance (Fig. S7 in the ESM). Furthermore, the BVO/FeCoMOF photoanode demonstrated a lower onset potential for water oxidation, indicating a more efficient separation and utilization of photogenerated charge carriers under mild bias conditions. The enhanced PEC performance can be attributed to the effective electronic coupling established between the amorphous FeCoMOF layer and the BVO substrate, as well as the improved surface charge transfer kinetics and the increased activity for the OER facilitated by the FeCoMOF layer. The electrochemical performance of the photoanode is also an important indicator reflecting its PEC water oxidation activity. Photoanodes with superior electrochemical properties typically demonstrate enhanced PEC water oxidation performance [40]. To distinguish the surface oxygen evolution catalytic role of FeCoMOF from its function in the p–n heterojunction, dark-state linear sweep voltammetry (LSV) measurements were carried out. Under dark conditions, no photogenerated charge carriers are involved; therefore, the measured current response mainly reflects the intrinsic oxygen evolution catalytic activity of the surface layer. As shown in Fig. 4(a) and Fig. S8 in the ESM, compared with bare BVO, the FeCoMOF-modified photoanode exhibits a higher current density and a lower onset overpotential. Notably, as the applied potential gradually increases, the current advantage of BVO/FeCoMOF over pristine BVO becomes progressively more pronounced, indicating that FeCoMOF can effectively reduce the kinetic barrier of the water oxidation reaction under higher overpotential conditions. Evidently, within the PEC operational potential range under illumination (around 1.23 V vs. RHE), the enhancement in photocurrent density of the BVO/FeCoMOF photoanode relative to bare BVO is significantly greater than the current increase observed under dark conditions. This result suggests that during the photoelectrochemical water oxidation process, the FeCoMOF layer not only provides surface catalytic sites for oxygen evolution but also synergistically interacts with BVO through heterojunction formation to promote the separation of photogenerated charge carriers and their interfacial injection, thereby jointly enhancing the overall PEC performance.

To further evaluate the oxygen evolution reaction kinetics, the Tafel slope analysis was performed based on the dark-state LSV curves. The Tafel slope reflects the intrinsic reaction kinetics of oxygen evolution, with a smaller value indicating faster reaction kinetics and more efficient interfacial charge transfer. As shown in Fig. S9 in the ESM, the BVO/FeCoMOF photoanode exhibits a markedly smaller Tafel slope (120 mV·dec^{-1}) than that of pristine BVO (199 mV·dec^{-1}), further confirming that the introduction of FeCoMOF significantly accelerates surface oxygen evolution kinetics [41]. In addition, the electrochemically active surface area (ECSA) of the photoanode was calculated from cyclic voltammetry (CV) curves (Fig. S10 in the ESM), which is positively correlated with the electrochemical double-layer capacitance (C_{dl}) [42]. The C_{dl}

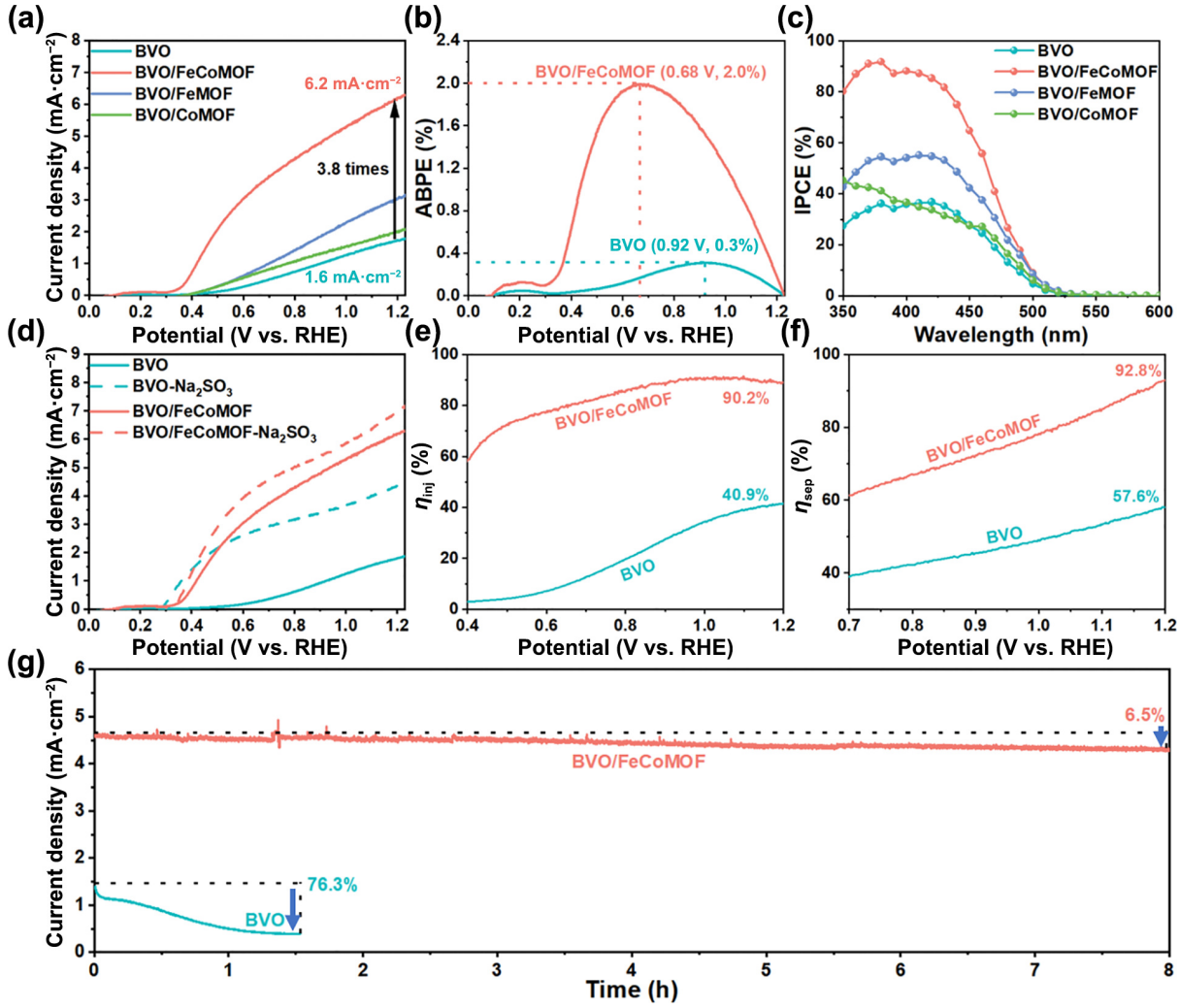

Figure 4 (a) LSV curves of PEC water oxidation illuminated by simulated sunlight (100 mW·cm^{-2}). (b) ABPE curves. (c) IPCE curves. (d) LSV curves (the dashed line represents the addition of 0.25M Na_2SO_3 solution). ((e) and (f)) Surface charge injection efficiency and charge separation efficiency for the BVO and BVO/FeCoMOF photoanodes. (g) *J*–*t* curves of the BVO and BVO/FeCoMOF photoanodes.

value of BVO/FeCoMOF is 0.22 mF·cm^{-2} (Fig. S11 in the ESM), significantly higher than that of pristine BVO (0.14 mF·cm^{-2}), indicating that the loading of FeCoMOF exposes a higher density of catalytic active sites, thereby enhancing the kinetics of water oxidation. Furthermore, static water contact angle measurements were employed to evaluate the water adsorption capability of the photoanodes. The water contact angle of bare BVO was measured to be 38.3°, indicating a moderate affinity toward water molecules. In contrast, the contact angle on BVO/FeCoMOF decreased markedly to 11.8° (Fig. S12 in the ESM), demonstrating a significant increase in hydrophilicity. The introduction of FeCoMOF altered the surface functional group composition (e.g., carboxyl groups), increasing surface polarity and consequently enhancing hydrophilicity. Stronger hydrophilicity allows the electrolyte solution to better wet the catalytic surface, facilitating the approach of water molecules to the reaction sites.

The applied bias photon-to-current efficiency (ABPE) and the incident photon-to-current efficiency (IPCE) are two critical metrics for assessing the PEC performance of photoelectrodes [43]. The ABPE reflects the net photocurrent produced by extracting electrons from the photoelectrode under an applied bias [44]. The ABPE of the prepared photoanodes was calculated from the LSV curves (Fig. 4(b)). The bare BVO exhibits a maximum ABPE of ~ 0.3% at 0.92 V vs. RHE. In contrast, the BVO/FeCoMOF composite achieves a significantly higher ABPE of 2.0%, with a reduced onset bias of 0.68 V vs. RHE, indicating that a higher ABPE can be achieved under a lower applied bias. The results indicate that the FeCoMOF modification significantly enhances the energy conversion efficiency of BVO, highlighting the potential of this composite structure for practical PEC applications. Figure 4(c) shows the IPCE spectra of the photoanodes under different wavelengths. All samples display an absorption edge at approximately 520 nm, which aligns with the UV–vis absorption results, suggesting that the primary role of the MOF is to regulate the interface and promote charge separation, rather than significantly enhancing the light absorption range. Benefiting from the synergistic effect between Fe and Co, the BVO/FeCoMOF photoanode shows a significantly enhanced IPCE in the visible region, achieving a maximum IPCE up to 90% at 370 nm, indicating a substantial enhancement in photon-to-current conversion efficiency.

To gain deeper insights into charge transfer and recombination behavior, the charge separation efficiency (η_{sep}) and the surface charge injection efficiency (η_{inj}) were calculated. η_{sep} represents the

percentage of photogenerated holes that reach the semiconductor–electrolyte interface (SEI) from the total number of photogenerated holes, while η_{inj} indicates the percentage of these holes that participate in the water oxidation reaction at the SEI [45]. In the LSV tests (Fig. 4(d)), 0.25 M Na_2SO_3 was added to the electrolyte as a hole scavenger to evaluate the charge injection and separation efficiencies, assuming a catalytic efficiency of 100% [46]. The charge injection efficiency of BVO increased from 40.9% to 90.2% after the loading of FeCoMOF (Fig. 4(e)). Figure 4(f) shows the charge separation efficiencies of BVO and BVO/FeCoMOF photoanodes. The pristine BVO exhibited a relatively low charge separation efficiency of 57.6% at 1.23 V vs. RHE, whereas the FeCoMOF-modified BVO showed an increased efficiency of 92.8%, indicating that FeCoMOF promoted charge transfer. This significant enhancement can be mainly attributed to the synergistic effects of the p–n heterojunction interface and the step-scheme type-II heterojunction, which together promote carrier separation and transfer while effectively suppressing surface charge recombination. Open-circuit photovoltage measurements were also conducted on the photoanodes. The difference in open-circuit potential (OCP) under dark and illuminated conditions (Δ_{OCP}) reflects the strength of the built-in electric field. A larger Δ_{OCP} indicates a stronger built-in electric field, which facilitates the separation and migration of photogenerated holes [41, 47]. The test results showed that the Δ_{OCP} of pristine BVO was 0.408 V (Fig. S13 in the ESM), while that of the BVO/FeCoMOF composite photoanode increased to 0.468 V, representing a significant enhancement over the former. The result indicates that the introduction of FeCoMOF enhances the strength of the interfacial electric field and optimizes the band structure at the semiconductor-electrolyte interface, thereby effectively suppressing the recombination of photogenerated charge carriers and improving hole utilization and PEC conversion efficiency.

The stability of the BVO photoanode primarily reflects its ability to resist photocorrosion, which is one of the intrinsic drawbacks of BVO. To evaluate stability, long-term photocurrent-time measurements were performed under continuous illumination at a constant potential, which was determined based on the potential associated with the maximum ABPE. As shown in Fig. 4(g), the photocurrent of the pristine BVO electrode exhibited a rapid decline in the initial stages of testing, indicating its susceptibility to photocorrosion during illumination. In contrast, the BVO/FeCoMOF photoanode exhibits excellent operational stability under continuous illumination for 8 h. Notably, the photoanode retains over 93.5% of its initial photocurrent after 8 h, indicating that the incorporation of FeCoMOF not only enhances the photocurrent density but also improves the interfacial resistance to photocorrosion, thereby strengthening the structural and electrochemical stability of the system. This stability performance is superior to that of most previously reported BVO-based photoanodes, highlighting the combined advantages of enhanced activity and long-term operational stability (Table S1 in the ESM). The production of H_2 and O_2 from the BVO/FeCoMOF photoanode was quantified at 1.23 V vs. RHE under AM 1.5 G illumination. As shown in Figs. S14 and S15 in the ESM, the amounts of H_2 and O_2 increased almost linearly with irradiation time during the 3-h operation. After 3 h, 265.9 μmol of H_2 and 129.8 μmol of O_2 were obtained, giving an H_2/O_2 molar ratio close to 2:1, which agrees well with the stoichiometry of overall water splitting. Based on the theoretical amounts derived from the passed charge, the Faradaic efficiencies for H_2 and O_2 were calculated to be 95.0% and 92.8%, respectively. The slightly lower Faradaic efficiency for O_2 compared to H_2, as well as the marginally higher amount of detected H_2, can be reasonably attributed to the higher solubility of O_2 in the aqueous electrolyte, which leads to partial dissolution of generated O_2 during collection, whereas H_2 has much lower solubility and is therefore more accurately detected. In addition, minor gas loss during long-term operation cannot be completely excluded despite careful sealing. Overall, the obtained Faradaic efficiencies demonstrate efficient charge utilization and are well within the range reported for comparable BVO-based photoanodes in the literature, supporting the reliability of the gas evolution measurements. To further elucidate the origin of the improved stability, the samples after the stability test were characterized by XRD, SEM, XPS, and FTIR. The XRD patterns (Fig. S16 in the ESM) reveal that the BVO/FeCoMOF photoanode after the stability test retained the characteristic monoclinic BVO diffraction peaks with sharp and well-defined profiles. Notably, no significant peak shift was observed, indicating that the crystalline structure remained intact during the prolonged PEC operation. The SEM image (Fig. S17 in the ESM) demonstrates that the electrode surface remained uniform after the stability test, with the FeCoMOF nanostructures still firmly attached to the BVO substrate, indicating that the heterojunction interface exhibits excellent structural robustness and adhesion. Furthermore, the FTIR spectra (Fig. S18 in the ESM) show that the characteristic vibration peaks corresponding to V–O bonds and organic ligands were preserved after the stability test, with no emergence of new peaks or significant peak shifts. XPS results (Fig. S19 in the ESM) indicate that the chemical composition of the sample remained nearly unchanged after the stability test. The above results confirm the robust structural and chemical stability of the BVO/FeCoMOF photoanode during long-term PEC operation.

2.4 Carrier dynamics analysis

To gain deeper insight into the origin of the enhanced PEC performance, the charge-transfer kinetics of the samples were systematically investigated. Fig. 5(a) and Fig. S20 in the ESM show the photoluminescence (PL) spectroscopy of BVO and BVO/FeCoMOF photoanodes. The pristine BVO exhibits a strong emission peak at 480 nm, which is indicative of significant recombination of photogenerated charge [48, 49]. Upon loading FeCoMOF onto BVO, the PL emission intensity decreases significantly, indicating that the incorporation of FeCoMOF effectively suppresses charge carrier recombination. Furthermore, to quantify the carrier lifetime, time-resolved photoluminescence (TRPL) spectra of the photoanodes were measured, and the decay curves were fitted accordingly [50]. The average carrier lifetime of pristine BVO is only 1.804 ns (Fig. 5(b)), whereas the carrier lifetime for BVO/FeCoMOF is significantly extended to 2.225 ns. This enhancement can be attributed to the strong internal electric field at the p–n heterojunction interface of BVO/FeCoMOF, which facilitates charge separation and suppresses recombination. Meanwhile, the stepwise type-II band alignment enables efficient and selective separation of electrons and holes, thereby effectively prolonging the carrier lifetime. The extended carrier lifetime is crucial for promoting interfacial water oxidation reactions.

Intensity-modulated photocurrent spectroscopy (IMPS) and intensity-modulated photovoltage spectroscopy (IMVS) are powerful techniques for investigating the charge carrier dynamics in

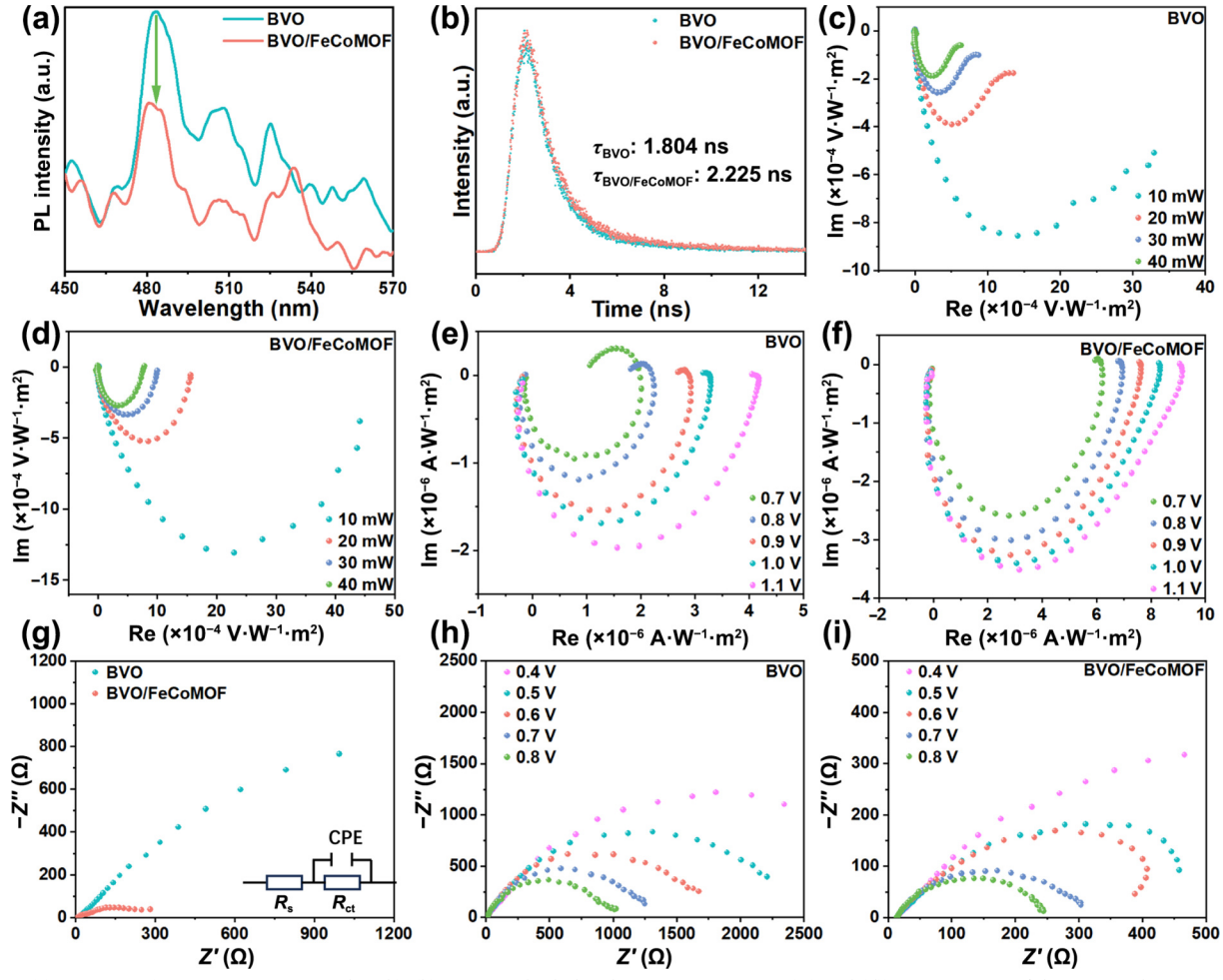

Figure 5 (a) PL spectra (405 nm excitation wavelength). (b) Time-resolved photoluminescence spectra. ((c) and (d)) IMVS spectra of the BVO and BVO/FeCoMOF photoanode. ((e) and (f)) IMPS spectra of the BVO and BVO/FeCoMOF photoanode. ((g)–(i)) Open-circuit impedance and *in-situ* impedance of the BVO and BVO/FeCoMOF photoanode.

photoanodes. IMVS is performed under open-circuit conditions, during which no significant water oxidation occurs at the photoanode surface [51], so the measurements primarily reflect the migration behavior of charge carriers within the bulk of the photoanode. As shown in Figs. 5(c) and 5(d), the IMVS curves of the photoanodes were obtained, and the photogenerated carrier lifetimes were calculated. Notably, the carrier lifetimes for all photoanodes decrease as light intensity increases (Fig. S21 in the ESM). Under the same illumination, the carrier lifetime of the BVO/FeCoMOF photoanode is significantly longer than that of the pristine BVO photoanode, indicating that FeCoMOF effectively promotes the separation and migration of photogenerated carriers. IMPS is conducted under short-circuit conditions, and an applied bias is required to facilitate the migration of photogenerated holes toward the electrolyte [52]. To quantify the impact of FeCoMOF on carrier transport, the carrier transit time was calculated. Longer transit time is indicative of higher recombination rates and lower transport rates. As shown in Figs. 5(e) and 5(f), the carrier transit time decreases significantly with increasing applied bias, demonstrating an enhancement in the migration ability of photogenerated holes. Under the same bias, the carrier transit time of the pristine BVO photoanode is larger than that of the BVO/FeCoMOF photoanode. Together with the extended carrier lifetimes observed from IMVS measurements, the IMPS and IMVS analyses reveal clear improvements in carrier transport and suppressed recombination behavior. These results directly correlate with the enhanced photocurrent density observed for the BVO/FeCoMOF photoanode, supporting the conclusion that the combined effect of the p–n heterojunction-induced internal electric field and the stepwise type-II band alignment facilitates more efficient charge separation and interfacial charge injection.

To gain deeper insight into the interfacial charge transfer processes of the photoanode, *in-situ* photoelectrochemical impedance spectroscopy (PEIS) measurements were conducted both at OCP (where no current flows through the system) and under various applied biases. The PEIS results obtained under OCP conditions represent the intrinsic interfacial charge transfer resistance in the absence of current driving, comprehensively reflecting the inherent ease of photogenerated carrier migration and interfacial reactions. As shown in Fig. 5(g), the Nyquist semicircle diameter of the BVO/FeCoMOF photoanode under OCP is markedly smaller than that of pristine BVO, indicating a lower interfacial charge transfer resistance even without external bias. This reduced impedance is indicative of more favorable interfacial charge transfer behavior, which is consistent with improved separation and migration of photogenerated carriers [28]. *In-situ* PEIS conducted under applied biases (Figs. 5(h) and 5(i), and Fig. S22 in the ESM) reveals the dynamic charge transfer processes of

the catalyst under actual PEC operating potentials. With increasing applied bias, the impedance of both BVO and BVO/FeCoMOF photoanodes gradually decreases, indicating that higher bias facilitates the charge separation and interfacial charge transfer. Notably, the impedance values of BVO/FeCoMOF remain lower than those of pristine BVO across the entire tested potential range. This trend suggests that the FeCoMOF modification promotes the interfacial charge transfer and reduces the interfacial resistance, which correlates well with the enhanced PEC performance observed under illumination.

To further elucidate the charge separation and transfer behavior, *in-situ* Kelvin probe force microscopy (KPFM) measurements were performed on pristine BVO and BVO/FeCoMOF photoanodes [34]. As shown in Figs. 6(a)–6(f), under dark conditions, the average surface potential of BVO photoanode was approximately −100 mV, which increased significantly to −50 mV upon the introduction of FeCoMOF layer. Under illumination, the surface potential of BVO photoanode further shifted to −30 mV, indicating the accumulation of photogenerated holes at the surface, whereas the average surface potential of BVO/FeCoMOF photoanode exhibited a significantly greater increase to 100 mV. The significant changes in potential indicate that BVO/FeCoMOF possesses superior photogenerated charge separation capability compared to bare BVO, highlighting the crucial role of the FeCoMOF overlayer in facilitating interfacial charge separation. Moreover, compared with the dark state, the positive shift in the surface potential of BVO/FeCoMOF under illumination confirms that FeCoMOF can effectively capture and store photogenerated holes from BVO, thereby accelerating the interfacial water oxidation reaction. Notably, such efficient hole extraction and rapid consumption also reduce the accumulation of high-energy photogenerated holes at the BVO surface, thereby suppressing continuous oxidative attack on the BVO lattice and mitigating photo-corrosion, which provides a reasonable explanation for the significantly improved long-term stability of the BVO/FeCoMOF photoanode. According to the above analysis, the charge transfer processes of the BVO and BVO/FeCoMOF photoanodes are illustrated in Figs. 6(g) and 6(h). Initially, the PEC water oxidation performance of the bare BVO photoanode is limited by poor charge separation, severe bulk and surface electron–hole recombination, and sluggish water oxidation kinetics (Fig. 6(g)). In sharp contrast, the BVO/FeCoMOF photoanode demonstrates significantly improved PEC conversion performance (Fig. 6(h)). Specifically, this enhancement is primarily attributed to the internal electric field formed at the BVO/FeCoMOF heterojunction interface, which drives photogenerated electrons and holes in opposite directions and suppresses their

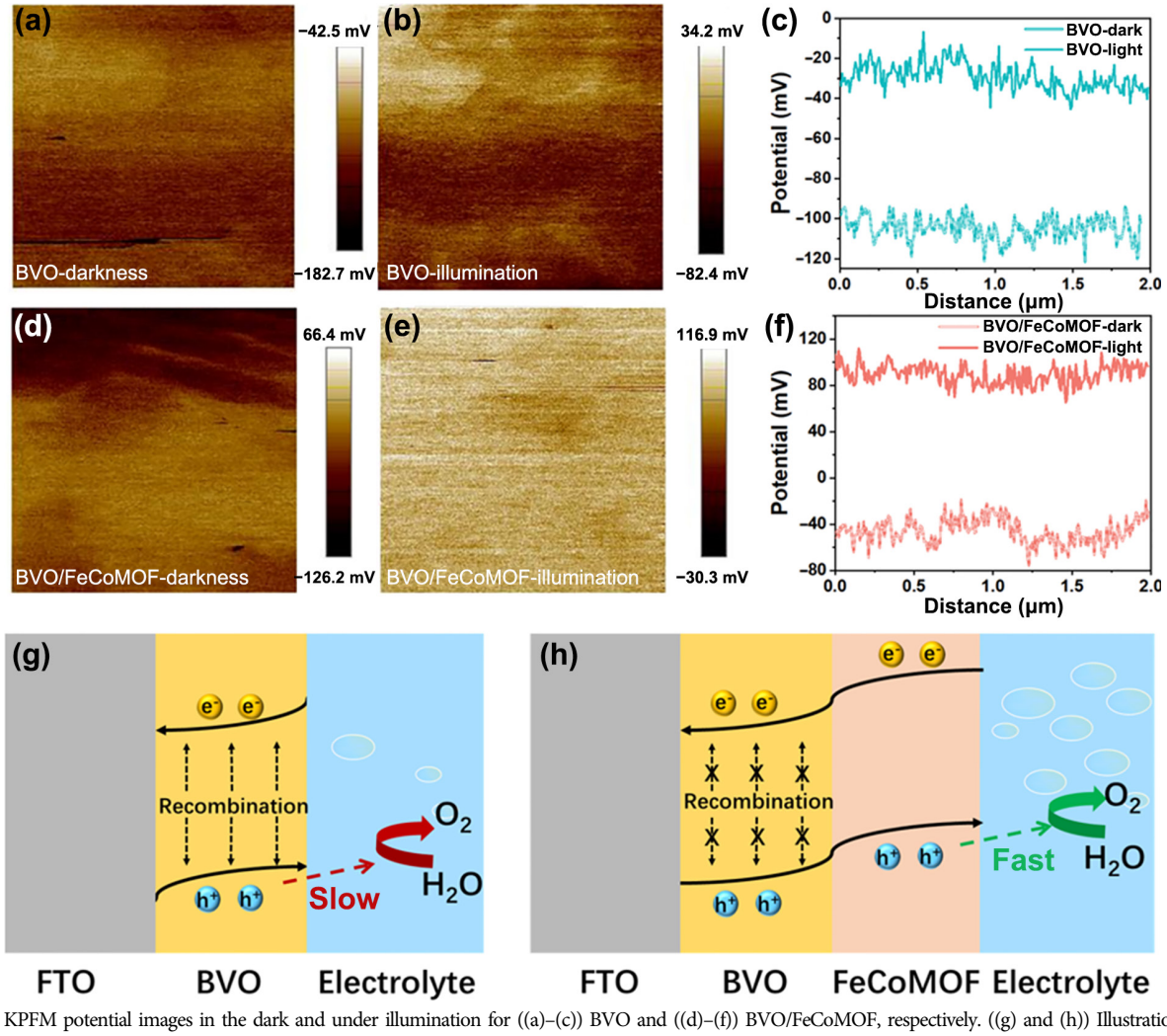

Figure 6 KPFM potential images in the dark and under illumination for ((a)–(c)) BVO and ((d)–(f)) BVO/FeCoMOF, respectively. ((g) and (h)) Illustrations of the charge transfer process for BVO and BVO/FeCoMOF photoanodes.

recombination. In addition, the stepwise type-II band alignment between BVO and FeCoMOF further enables efficient and selective separation of charge carriers. The FeCoMOF layer provides abundant unsaturated metal sites and flexible coordination environments, which facilitate interfacial charge transfer and accelerate surface oxygen evolution kinetics.

3 Conclusions

In summary, this work reports the construction of BVO photoanodes loaded with FeCoMOF. By forming a p–n heterojunction interface and realizing a stepwise type-II band alignment, the separation and migration of photogenerated charge carriers were effectively regulated. Systematic characterizations and PEC measurements demonstrate that the FeCoMOF loading not only provides a high surface area, but also generates a strong internal electric field at the interface, thereby significantly prolonging carrier lifetime, suppressing electron–hole recombination, and enhancing interfacial charge injection of photogenerated carriers. Under visible-light illumination, the photoanodes exhibit markedly improved photocurrent density and PEC efficiency, clearly validating that the synergistic effect of the p–n heterojunction and type-II band structure is the key mechanism for enhancing PEC performance. This study provides a new strategy for the heterojunction design of metal oxide photoanodes, demonstrating that rational loading of metal-organic frameworks combined with band structure engineering can achieve efficient management of photogenerated carriers, offering a feasible approach for solar-driven water oxidation and other PEC applications.

Electronic Supplementary Material: Supplementary material is available in the online version of this article at https://doi.org/10.26599/NR.2026.94908454.

Data availability

All data needed to support the conclusions in the paper are presented in the manuscript and the Electronic Supplementary Material. Additional data related to this paper may be requested from the corresponding author upon request.

Acknowledgements

This work was financially supported by the National Key Research and Development Program of China (No. 2023YFA1507204), the National Natural Science Foundation of China (Nos. 22539002 and 22271081), Natural Science Foundation of Heilongjiang Province (No. PL2024B017), and the Heilongjiang University Excellent Youth Foundation.

Declaration of competing interest

All the contributing authors report no conflict of interests in this work.

Author contribution statement

Q. Y. C.: Data acquisition, data curation, writing manuscript, experimental design. Y. H.: Data curation, validation. J. K. G.: Formal analysis. J. Z.: Data curation, validation. D. X. W.: Formal analysis, methodology. C. G. T.: Data analysis, methodology. A. P. W.: Project administration, experimental design, writing manuscript. H. G. F.: Project administration, funding acquisition, writing manuscript. All the authors have approved the final manuscript.

Use of AI statement

During the preparation of this work, the author(s) used ChatGPT in order to polish the English language and improve the writing of the manuscript. After using this tool, the author(s) reviewed and edited the content as needed and take full responsibility for the content of the publication.

References

[1] Wu, S. M.; Wu, L.; Denisov, N.; Badura, Z.; Zoppellaro, G.; Yang, X. Y.; Schmuki, P. Pt single atoms on TiO_2 can catalyze water oxidation in photoelectrochemical experiments. *J. Am. Chem. Soc.* **2024**, *146*, 16363–16368.

[2] Zhou, X.; Fu, B. H.; Li, L. J.; Tian, Z.; Xu, X. K.; Wu, Z. H.; Yang, J.; Zhang, Z. H. Hydrogen-substituted graphdiyne encapsulated cuprous oxide photocathode for efficient and stable photoelectrochemical water reduction. *Nat. Commun.* **2022**, *13*, 5770.

[3] Miao, J. M.; Lin, C.; Yuan, X. J.; An, Y.; Yang, Y.; Li, Z. S.; Zhang, K. Supramolecular catalyst with $[FeCl_4]$ unit boosting photoelectrochemical seawater splitting via water nucleophilic attack pathway. *Nat. Commun.* **2024**, *15*, 2023.

[4] He, Y.; Wu, A. P.; Wang, N.; Xie, Y.; Tian, C. G.; Fu, H. G. Porous S-doped carbon nitride foam with accelerated charge dynamics for synchronous photocatalytic hydrogen production and highly selective oxidation of amines. *Nano Res.* **2024**, *17*, 6860–6869.

[5] Ding, C. M.; Shi, J. Y.; Wang, Z. L.; Li, C. Photoelectrocatalytic water splitting: Significance of cocatalysts, electrolyte, and interfaces. *ACS Catal.* **2017**, *7*, 675–688.

[6] Zhang, X. M.; Zhai, P. L.; Zhang, Y. X.; Wu, Y. Z.; Wang, C.; Ran, L.; Gao, J. F.; Li, Z. W.; Zhang, B.; Fan, Z. Z. et al. Engineering single-atomic Ni-N_4-O sites on semiconductor photoanodes for high-performance photoelectrochemical water splitting. *J. Am. Chem. Soc.* **2021**, *143*, 20657–20669.

[7] Meng, Q. J.; Zhang, B. B.; Fan, L. Z.; Liu, H. D.; Valvo, M.; Edström, K.; Cuartero, M.; de Marco, R.; Crespo, G. A.; Sun, L. C. Efficient $BiVO_4$ photoanodes by postsynthetic treatment: Remarkable improvements in photoelectrochemical performance from facile borate modification. *Angew. Chem., Int. Ed.* **2019**, *58*, 19027–19033.

[8] Yang, J.; Deng, C. Y.; Lei, Y.; Duan, M. Y.; Yang, Y. S.; Chen, X. R.; Yang, S. P.; Li, J. K.; Sheng, H.; Shi, W. Q. et al. Fe-N co-doped $BiVO_4$ photoanode with record photocurrent for water oxidation. *Angew. Chem., Int. Ed.* **2025**, *64*, e202416340.

[9] He, B.; Cao, Y.; Lin, K. J.; Wu, M. J.; Zhu, Y. H.; Cui, X.; Hu, L.; Yang, Y. K.; Liu, X. Q. Enhanced bulk and interfacial charge transfer in Fe: $VOPO_4$ modified Mo: $BiVO_4$ photoanodes for photoelectrochemical water splitting. *eScience* **2025**, *5*, 100242.

[10] Dai, D. J.; Wang, P.; Bao, X. L.; Xu, Y. Y.; Wang, Z. Q.; Guo, Y. H.; Wang, Z. Y.; Zheng, Z. K.; Liu, Y. Y.; Cheng, H. F. et al. g-C_3N_4/ITO/Co-$BiVO_4$ Z-scheme composite for solar overall water splitting. *Chem. Eng. J.* **2022**, *433*, 134476.

[11] Xia, S. H.; Xu, F. H.; Weng, B. C. An optimized heterointerface of $BiVO_4$/C_3N_4 by Co single atom and F-doping for boosting photoelectrochemical water splitting. *J. Mater. Chem. A* **2024**, *12*, 4635–4642.

[12] Zhang, W.; Tian, M.; Jiao, H. M.; Jiang, H. Y.; Tang, J. W. Conformal $BiVO_4$/WO_3 nanobowl array photoanode for efficient photoelectrochemical water splitting. *Chin. J. Catal.* **2022**, *43*, 2321–2331.

[13] Xu, S.; Fu, D. F.; Song, K.; Wang, L.; Yang, Z. B.; Yang, W. Y.; Hou,

H. L. One-dimensional $WO_3/BiVO_4$ heterojunction photoanodes for efficient photoelectrochemical water splitting. *Chem. Eng. J.* **2018**, *349*, 368–375.

[14] Bai, S. L.; Chu, H. M.; Xiang, X.; Luo, R. X.; He, J.; Chen, A. F. Fabricating of $Fe_2O_3/BiVO_4$ heterojunction based photoanode modified with NiFe-LDH nanosheets for efficient solar water splitting. *Chem. Eng. J.* **2018**, *350*, 148–156.

[15] Xu, L.; Li, M. H.; Zhao, F. M.; Quan, J. J.; Ning, X. M.; Chen, P.; An, Z. W.; Chen, X. B. Low oxidation state engineering in transition metal-based interfacial regulation layer accelerates charge transfer kinetics toward enhanced photoelectrochemical water splitting. *Appl. Catal. B: Environ. Energy* **2024**, *359*, 124503.

[16] Yin, H.; Guo, Y. Z.; Zhang, N.; Wang, Y. Y.; Zhang, S. R.; Jiang, R. B. Boosting photoelectrochemical water oxidation by sandwiching gold nanoparticles between $BiVO_4$ and NiFeOOH. *J. Mater. Chem. A* **2023**, *11*, 24239–24247.

[17] Lin, J. Y.; Li, X.; Wang, Z. L.; Liu, R. L.; Pan, H.; Zhao, Y. X.; Kong, L. T.; Li, Y.; Zhu, S. M.; Wang, L. Z. Organic ligand nanoarchitectonics for $BiVO_4$ photoanodes surface passivation and cocatalyst grafting. *Nano Res.* **2024**, *17*, 3667–3674.

[18] Zhu, S. S.; Zhang, Y.; Zou, Y.; Guo, S. Y.; Liu, H.; Wang, J. J.; Braun, A. $Cu_2S/BiVO_4$ heterostructure photoanode with extended wavelength range for efficient water splitting. *J. Phys. Chem. C* **2021**, *125*, 15890–15898.

[19] Geng, H. M.; Ying, P. Z.; Zhao, Y. L.; Gu, X. Q. Cactus shaped $FeOOH/Au/BiVO_4$ photoanodes for efficient photoelectrochemical water splitting. *Int. J. Hydrogen Energy* **2021**, *46*, 35280–35289.

[20] Wang, Q. J.; Oldham, L. I.; Giner-Requena, A.; Wang, Z. Y.; Benetti, D.; Montilla-Verdú, S.; Chen, R.; Du, D. F.; Lana-Villarreal, T.; Aschauer, U. et al. Enhancing photoelectrochemical water oxidation using ferromagnetic materials and magnetic fields. *J. Am. Chem. Soc.* **2024**, *146*, 34681–34689.

[21] Chen, X. C.; Li, X.; Peng, Y. M.; Yang, H.; Tong, Y. X.; Balogun, M. S.; Huang, Y. C. Tailoring carrier dynamics of $BiVO_4$ photoanode via dual incorporation of Au and $Co(OH)_x$ cooperative modification for photoelectrochemical water splitting. *Adv. Funct. Mater.* **2025**, *35*, 2416091.

[22] He, B.; Cao, Y.; Lin, K. J.; Wang, Y.; Li, Z.; Yang, Y. K.; Zhao, Y. L.; Liu, X. Q. Strong interactions between Au nanoparticles and $BiVO_4$ photoanode boosts hole extraction for photoelectrochemical water splitting. *Angew. Chem., Int. Ed.* **2024**, *63*, e202402435.

[23] Long, M. C.; Jiang, J. J.; Li, Y.; Cao, R. Q.; Zhang, L. Y.; Cai, W. M. Effect of gold nanoparticles on the photocatalytic and photoelectrochemical performance of Au modified $BiVO_4$. *Nano-Micro Lett.* **2011**, *3*, 171–177.

[24] Xie, J. L.; Yang, P. P.; Tang, C.; Chen, T.; Zhong, C. Y.; Wang, L. L.; Huang, Y. L. High-quality coating of conformal and oriented metal-organic framework cocatalyst layer for efficient photoelectrocatalysis. *Adv. Mater. Interfaces* **2021**, *8*, 2101069.

[25] Zhong, S. M.; Kang, B. K.; Cheng, X. X.; Chen, P. L.; Fang, B. Z. Construction of a Co-MOF/MXene/$BiVO_4$ composite photoanode for efficient photoelectrochemical water splitting. *ACS Sustain. Chem. Eng.* **2024**, *12*, 1233–1246.

[26] Pai, H.; Kuo, T. R.; Chung, R. J.; Kubendhiran, S.; Yougbaré, S.; Lin, L. Y. Enhanced photocurrent density for photoelectrochemical catalyzing water oxidation using novel W-doped $BiVO_4$ and metal organic framework composites. *J. Colloid Interface Sci.* **2022**, *624*, 515–526.

[27] Pan, J. B.; Wang, B. H.; Wang, J. B.; Ding, H. Z.; Zhou, W.; Liu, X.; Zhang, J. R.; Shen, S.; Guo, J. K.; Chen, L. et al. Activity and stability boosting of an oxygen-vacancy-rich $BiVO_4$ photoanode by NiFe-MOFs thin layer for water oxidation. *Angew. Chem., Int. Ed.* **2021**, *60*, 1433–1440.

[28] Zhang, Y.; Huang, Y.; Zhu, S. S.; Liu, Y. Y.; Zhang, X.; Wang, J. J.; Braun, A. Covalent S–O bonding enables enhanced photoelectrochemical performance of Cu_2S/Fe_2O_3 heterojunction for water splitting. *Small* **2021**, *17*, 2100320.

[29] Xiong, X. Q.; Zhang, C. Q.; Zhang, X.; Fan, L. Y.; Zhou, L. J.; Chu, Y. X.; Huang, W. Y.; Wu, C. L.; Li, J. S.; Yang, X. G. et al. Uniformly citrate-assisted deposition of small-sized FeOOH on $BiVO_4$ photoanode for efficient solar water oxidation. *Electrochim. Acta* **2021**, *389*, 138795.

[30] Xiong, X. Q.; Wong, N. H.; Ernawati, L.; Sunarso, J.; Zhang, X.; Jin, Y. X.; Han, D. M.; Wu, C. L.; Yu, B. B.; Yang, X. G. et al. Revealing the enhanced photoelectrochemical water oxidation activity of Fe-based metal-organic polymer-modified $BiVO_4$ photoanode. *J. Colloid Interface Sci.* **2023**, *644*, 533–545.

[31] Chen, Y. J.; Wang, N.; Hu, W. C.; Komarneni, S. *In situ* construction of porous Ni/Co-MOF@Carbon cloth electrode with honeycomb-like structure for high-performance energy storage. *J. Porous Mater* **2019**, *26*, 921–929.

[32] Zhou, T. S.; Li, L.; Li, J. H.; Wang, J. C.; Bai, J.; Xia, L. G.; Xu, Q. J.; Zhou, B. X. Electrochemically reduced TiO_2 photoanode coupled with oxygen vacancy-rich carbon quantum dots for synergistically improving photoelectrochemical performance. *Chem. Eng. J.* **2021**, *425*, 131770.

[33] Luo, Y. D.; Shi, G. Y.; Yu, S. H.; Liu, Z. T.; Yin, J. W.; Xue, M. S.; Sun, Q.; Shen, F. F.; Li, X. B.; Yin, Z. Z. et al. Novel MIL-88B(Fe)/ZnTi-LDH high-low junctions for adsorption and photodegradation of tetracycline: Characteristics, performance, and mechanisms. *Chem. Eng. J.* **2023**, *473*, 145198.

[34] Chen, X. T.; Zhen, C.; Li, J. J.; Qiu, J. H.; Li, N.; Jia, N.; Liu, G. Engineering facet-dependent interface charge transfer in liquid metal-embraced $BiVO_4$ photoelectrodes for efficient photoelectrochemical water splitting. *Adv. Funct. Mater.* **2024**, *34*, 2409566.

[35] Liu, Y.; Zhang, Z. Y.; Wang, K.; Tan, X. L.; Chen, J. R.; Ren, X. L.; Jiang, F. Efficient $BiVO_4$ photoanode with an excellent hole transport layer of CuSCN for solar water oxidation. *Adv. Energy Mater.* **2024**, *14*, 2304223.

[36] Zhu, S. C.; Wang, Z. C.; Tang, B.; Liang, H.; Liu, B. J.; Li, S.; Chen, Z. X.; Cheng, N. C.; Xiao, F. X. Progressively stimulating carrier motion over transient metal chalcogenide quantum dots towards solar-to-hydrogen conversion. *J. Mater. Chem. A* **2022**, *10*, 11926–11937.

[37] Kim, D. W.; Riha, S. C.; DeMarco, E. J.; Martinson, A. B. F.; Farha, O. K.; Hupp, J. T. Greenlighting photoelectrochemical oxidation of water by iron oxide. *ACS Nano* **2014**, *8*, 12199–12207.

[38] Ren, S. J.; Sun, M.; Guo, X. T.; Liu, X. H.; Zhang, X. Y.; Wang, L. Interface-confined surface engineering via photoelectrochemical etching toward solar neutral water splitting. *ACS Catal.* **2022**, *12*, 1686–1696.

[39] Sun, Y. S. Y.; Li, H.; Hu, Y.; Wang, J. N.; Li, A. M.; Corvini, P. F. X. Single-atomic ruthenium coupling with NiFe layered double hydroxide *in-situ* growth on $BiVO_4$ photoanode for boosting photoelectrochemical water splitting. *Appl. Catal. B: Environ.* **2024**, *340*, 123269.

[40] Xiang, K.; Wu, D.; Deng, X. H.; Li, M.; Chen, S. Y.; Hao, P. P.; Guo, X. F.; Luo, J. L.; Fu, X. Z. Boosting H_2 generation coupled with selective oxidation of methanol into value-added chemical over cobalt hydroxide@hydroxysulfide nanosheets electrocatalysts. *Adv. Funct. Mater.* **2020**, *30*, 1909610.

[41] Zhang, Y. J.; Xu, L. C.; Liu, B. Y.; Wang, X.; Wang, T. S.; Xiao, X.; Wang, S. C.; Huang, W. Engineering $BiVO_4$ and oxygen evolution cocatalyst interfaces with rapid hole extraction for photoelectrochemical water splitting. *ACS Catal.* **2023**, *13*, 5938–5948.

[42] He, Y. X.; Hu, Y. W.; Zhu, Z. X.; Li, J. Q.; Huang, Y. C.; Zhang, S. G.; Balogun, M. S.; Tong, Y. X. High-performance multidimensional-structured N-doped nickel modulated Mo_2N/FeO_xN_y bifunctional electrocatalysts for efficient alkaline seawater splitting. *Chem. Eng. J.* **2024**, *489*, 151348.

[43] Feng, J. Y.; Huang, H. T.; Guo, W. X.; Xu, X. M.; Yao, Y. F.; Yu, Z. T.; Li, Z. S.; Zou, Z. G. Evaluating the promotional effects of WO_3 underlayers in $BiVO_4$ water splitting photoanodes. *Chem. Eng. J.*

2021, *417*, 128095.

[44] Zhang, Y.; Bai, J.; Wang, J. C.; Chen, S.; Zhu, H.; Li, J. H.; Li, L. S.; Zhou, T. S.; Zhou, B. X. *In-situ* and synchronous generation of oxygen vacancies and FeO_x OECs on $BiVO_4$ for ultrafast electron transfer and excellent photoelectrochemical performance. *Chem. Eng. J.* **2020**, *401*, 126134.

[45] Gao, R. T.; Wang, L. Stable cocatalyst-free $BiVO_4$ photoanodes with passivated surface states for photocorrosion inhibition. *Angew. Chem., Int. Ed.* **2020**, *59*, 23094–23099.

[46] Wang, Y. Y.; Huang, J. C.; Chen, Y. X.; Yang, H.; Ye, K. H.; Huang, Y. C. Modulating built-in electric field via Bi–VO_4–Fe interfacial bridges to enhance charge separation for efficient photoelectrochemical water splitting. *J. Colloid Interface Sci.* **2024**, *672*, 12–20.

[47] Hegner, F. S.; Herraiz-Cardona, I.; Cardenas-Morcoso, D.; López, N.; Galán-Mascarós, J. R.; Gimenez, S. Cobalt hexacyanoferrate on $BiVO_4$ photoanodes for robust water splitting. *ACS Appl. Mater. Interfaces* **2017**, *9*, 37671–37681.

[48] Zhang, J.; He, Y.; Shi, Y.; Wang, N.; Wu, B. G.; Xia, S. X.; Wang, D. X.; Tian, C. G.; Wu, A. P.; Fu, H. G. Fe/$ZnIn_2S_4$/Ni micro heterojunctions with enhanced charge transfer for efficient photocatalytic hydrogen and imine production. *Nano Res.* **2025**, *18*, 94907595.

[49] Li, C. Q.; Wang, J. J. Copper sulfide based photocatalysts, electrocatalysts and photoelectrocatalysts: Innovations in structural modulation and application. *Small* **2024**, *20*, 2404798.

[50] Ai, Y. T.; Hu, J. J.; Xiong, X. Q.; Carabineiro, S. A. C.; Li, Y. S.; Sirotkin, N.; Agafonov, A.; Lv, K. L. Synergistic interfacial engineering of a S-scheme ZnO/In_2S_3 photocatalyst with S–O covalent bonds: A dual-functional advancement for tetracycline hydrochloride degradation and H_2 evolution. *Appl. Catal. B: Environ. Energy* **2024**, *353*, 124098.

[51] Li, Y.; Dai, X. Y.; Bu, Y. Y.; Zhang, H. Z.; Liu, J.; Yuan, W. Y.; Guo, X. H.; Ao, J. P. Photoelectrochemical performance improving mechanism: Hybridization appearing at the energy band of $BiVO_4$ photoanode by doped quantum layers modification. *Small* **2022**, *18*, 2200454.

[52] Gao, M. Z.; Nguyen, N. T.; Gao, R. T.; Liu, X. H.; Zhang, X. Y.; Wang, L. Engineering single Pt atoms on hybrid amorphous/crystalline CoFe layered double hydroxide accelerates the charge transfer for solar water splitting. *Appl. Catal. B: Environ.* **2023**, *336*, 122920.

This is an open access article under the terms of the Creative Commons Attribution 4.0 International License (CC BY 4.0, https://creativecommons.org/licenses/by/4.0/).

© The Author(s) 2026. Published by Tsinghua University Press.